Nature Geoscience
December 2019, Volume 12 Issue 12 Pages 995-1000
https://doi.org/10.1038/s41561-019-0476-6
https://archimer.ifremer.fr/doc/00589/70156/

Archimer
https://archimer.ifremer.fr

Resupply of mesopelagic dissolved iron controlled by particulate iron composition

Bressac M. [1, 2, *] , Guieu C. [2, 3], Ellwood M. J. [4], Tagliabue A. [5], Wagener T. [6], Laurenceau-Cornec E. C. [1], Whitby Hannah [7], Sarthou Geraldine [9], Boyd P. W. [1, 8]

[1] Institute for Marine and Antarctic Studies, University of Tasmania, Hobart, Tasmania, Australia
[2] Sorbonne Université, CNRS, Laboratoire d'Océanographie de Villefranche, LOV, Villefranche-sur-Mer, France
[3] The Center for Prototype Climate Modeling, New York University in Abu Dhabi, Abu Dhabi, United Arab Emirates
[4] Research School of Earth Sciences, Australian National University, Canberra, Australian Capital Territory, Australia
[5] Department of Earth Ocean and Ecological Sciences, School of Environmental Sciences, University of Liverpool, Liverpool, UK
[6] Aix Marseille Université, CNRS, IRD, Université de Toulon, MIO UM 110, Marseille, France
[7] UMR 6539/LEMAR/IUEM, CNRS, UBO, IRD, Ifremer, Technopôle Brest Iroise, Plouzané, France
[8] Antarctic Climate and Ecosystems Collaborative Research Center, University of Tasmania, Hobart, Tasmania, Australia
[9] UMR 6539/LEMAR/IUEM, CNRS, UBO, IRD, Ifremer, Technopôle Brest Iroise, Plouzané, France

* Corresponding author : M. Bressac, email address : matthieu.bressac@utas.edu.au

Abstract :

The dissolved iron supply controls half of the oceans' primary productivity. Resupply by the remineralization of sinking particles, and subsequent vertical mixing, largely sustains this productivity. However, our understanding of the drivers of dissolved iron resupply, and their influence on its vertical distribution across the oceans, is still limited due to sparse observations. There is a lack of empirical evidence as to what controls the subsurface iron remineralization due to difficulties in studying mesopelagic biogeochemistry. Here we present estimates of particulate transformations to dissolved iron, concurrent oxygen consumption and iron-binding ligand replenishment based on in situ mesopelagic experiments. Dissolved iron regeneration efficiencies (that is, replenishment over oxygen consumption) were 10- to 100-fold higher in low-dust subantarctic waters relative to higher-dust Mediterranean sites. Regeneration efficiencies are heavily influenced by particle composition. Their make-up dictates ligand release, controls scavenging, modulates ballasting and may lead to the differential remineralization of biogenic versus lithogenic iron. At high-dust sites, these processes together increase the iron remineralization length scale. Modelling reveals that in oceanic regions near deserts, enhanced lithogenic fluxes deepen the ferricline, which alter the vertical patterns of dissolved iron replenishment, and set its redistribution at the global scale. Such wide-ranging regeneration efficiencies drive different vertical patterns in dissolved iron replenishment across oceanic provinces.

Please note that this is an author-produced PDF of an article accepted for publication following peer review. The definitive publisher-authenticated version is available on the publisher Web site.

Globally, the productivity of major phytoplankton groups, including diatoms and diazotrophs, is set by dissolved iron (DFe) supply[1]. Twenty years of research has revealed diverse modes of DFe supply, from dust to hydrothermal vents, and their regional influences[2,3]. Iron biogeochemistry is a rapidly evolving field, driving the development of global modelling initiatives[4]. However, iron cycling in the oceans' interior, a fundamental component of iron biogeochemistry[5,6], represents a major unknown, and critically is hindering model development[7].

Deep winter mixing is a key vector in the annual resupply of upper ocean DFe stocks[8]. At depth, DFe is replenished via biotic (e.g., microbial solubilization) and abiotic (e.g., dissolution) transformations (also termed remineralization or replenishment here) of particulate Fe (PFe)[7]. To date, internal iron cycling has been investigated using three distinctive approaches, each of which has improved it's representation in biogeochemical models[9-11]. Firstly, studies deploying trace metal-clean multi-depth sediment traps, in regions dominated by biogenic PFe, provided initial evidence of subsurface decoupling in PFe remineralization relative to phosphorus (P), carbon (C) or nitrogen[12-15]. Second, bacterially-mediated PFe remineralization – suppressed in sediment trap studies due to preservatives – was investigated in shipboard time-series incubations of resuspended mesopelagic particles in which the release of DFe and Fe-binding ligands resulted from particle degradation[9,16]. Third, dust addition experiments within nearshore 15 m deep mesocosms demonstrated that lithogenic Fe, conventionally viewed as a major source of external Fe to surface waters[1,2,17], can either release (dissolution) or remove (scavenging) DFe depending on the initial biogeochemical conditions[18-20].

These three approaches to internal iron cycling targeted different processes, such as ligand and DFe release[9,16], patterns in PFe flux attenuation[12-15], or scavenging and dissolution[18-20]. However, it is difficult to compare the findings of these studies as they each sampled particle assemblages with differing contributions from biogenic and lithogenic iron. Hence, no study so far has examined the relative role of the different processes associated with biogenic versus lithogenic Fe on internal iron cycling. The hypothesis[9] that the composition of particles will largely determine mesopelagic patterns of DFe replenishment remains untested due to difficulties in studying this stratum[21] and in discriminating between biogenic and lithogenic

PFe within sinking particles[7]. Here, we overcame both limitations by targeting regions dominated by biogenic, a mix of biogenic/lithogenic, or lithogenic sinking PFe, and applying a novel *in situ* particle interceptor/incubator – RESPIRE[22] – to iron biogeochemistry to concurrently elucidate the roles of biogenic and lithogenic PFe and their fate within the upper mesopelagic zone (~100-200 m depth).

Contrasting biogeochemical areas – Mesopelagic Fe cycling was studied using a trace metal-clean version of RESPIRE (TM-RESPIRE; Supplementary-Fig. 1) on a surface-tethered free-drifting mooring to non-intrusively intercept settling particles, and then immediately (i.e., at the end of the 1-2 d collection period) incubate them within this device at *in situ* pressure and temperature. RESPIRE[22] provides rates of remineralization by particle-attached bacteria based on an oxygen consumption time-series (Fig. 1a-b). TM-RESPIRE provides the PFe/P/C sinking fluxes and associated DFe/P/C replenishment rates along with concurrent release of iron-binding ligands. In doing so, the TM-RESPIRE approach (along with subsequent analysis to estimate scavenging) combines all three previous approaches and permits the investigation *in situ* of the different processes driving the Fe remineralization and their interplay.

RESPIRE and TM-RESPIRE were deployed (vertically separated by <20 m; Methods) at 1 or 2 depths in the upper mesopelagic (110-200 m depth) during GEOTRACES process studies in the Subantarctic Zone (SAZ) and Mediterranean Sea (Supplementary-Table 1; Methods). These sites span wide-ranging dust deposition and productivity regimes (Fig. 1c). At SAZ, High-Nitrate-Low-Chlorophyll (HNLC) surface waters are characterized by low dust deposition and biologically-limiting DFe levels[24]. In contrast, Fe-rich oligotrophic waters of the Eastern Mediterranean (ION site) encounter intense Saharan dust deposition event[23]. In

addition, a site within the Algerian basin (Western Mediterranean, ALG site) was selected since it had intermediate characteristics between these end-members (Fig. 1c).

These site-specific characteristics were reflected in the widely-differing particulate organic carbon (POC) and PFe sinking fluxes (Fig. 2; Supplementary-Table 1). SAZ had low POC fluxes (0.9-1.2 mmol m^{-2} d^{-1}), but in contrast to the seasonal biological trends evident in Fig. 1c, ~4-fold higher POC fluxes were measured at ION and ALG relative to SAZ, suggesting that a higher proportion of productivity was exported at these higher dust sites. This trend was probably due to lithogenic ballasting which is often associated with a high proportion of the POC export in the Mediterranean Sea[25,26]. PFe fluxes at the Mediterranean sites were also ~15-fold higher (8.0-12.5 μmol m^{-2} d^{-1} at 115 m depth) relative to the Subantarctic. This order-of-magnitude difference was driven by dust-derived lithogenic material (Supplementary-Fig. 2b and f), a major constituent of Mediterranean sinking fluxes[26] but negligible at SAZ[27]. Indeed, the Fe/C ratio of the sinking particles, a proxy of the biogenic:lithogenic PFe (Methods), ranged >30-fold (~460-13970 μmol/mol) confirming the SAZ site as the low lithogenic Fe end member (Fig. 3b-c). At ALG and ION, contrasting POC and PFe flux attenuation patterns were evident, with PFe increasing with depth while a 3-fold attenuation of POC flux occurred between 115-195 m depth (Fig. 2). Consequently, a decrease in the relative proportion of biogenic PFe occurred over this stratum, evident by increased Fe/C ratios (Fig. 3b-c).

Mesopelagic bacterial remineralization – Oxygen-based remineralization rates were correlated linearly to the POC concentrations within the RESPIRE (i.e., the intercepted POC flux; Fig. 3a). The absence of significant relationship(s) with other flux characteristics (Supplementary-Fig. 2a-d), reveals that POC exerted a first-order control on remineralization

rates. To assess whether DFe replenishment is largely driven by microbial solubilization of biogenic Fe in settling particles, we investigated trends in Fe regeneration efficiency ($R_{Fe/O2}$). Both site-specific and water-column processes contributed to the wide range of $R_{Fe/O2}$ (Fig. 3b). High $R_{Fe/O2}$ efficiencies were observed at the SAZ site (148-421 μmol/mol) but were one- to two-orders of magnitude lower at both Mediterranean sites. These trends in $R_{Fe/O2}$ are consistent with vertical DFe stocks increasing with depth at SAZ, and in contrast decreasing at the Mediterranean sites (Supplementary-Fig. 3). Similarly, replenishment rates of P and C were highest at SAZ (Supplementary-Table 2). Although the present study offers a snapshot of the annual cycle of mesopelagic remineralization, our observations are consistent with high-latitude studies characterized as sites with relatively labile particles prone to microbially-mediated remineralization[28,29].

Despite the complex transformations that characterize the internal cycle of Fe, a strong inverse relationship is observed between $R_{Fe/O2}$ and the composition of the PFe flux estimated from the particulate Fe/C ratio (Fig. 3b). Critically, this inverse relationship reveals that $R_{Fe/O2}$ is not determined by the magnitude of the PFe flux but rather by its particle composition (Supplementary-Fig. 2g-h). Furthermore, this negative relationship strongly suggests that biogenic PFe is efficiently regenerated while the dissolution of lithogenic PFe (predominant at the Mediterranean sites; Fig. 2) takes place at much lower rates, corroborating 1D model simulations showing that biogenic and lithogenic PFe fluxes exhibit distinctly different vertical attenuation[9].

Drivers of mesopelagic iron remineralization – To develop a better understanding of the drivers of mesopelagic iron biogeochemistry, $R_{Fe/O2}$ was converted into a Fe/C regeneration ratio ($R_{Fe/C}$; Methods) and compared with the Fe/C and biogenic Fe/C (Fe_{bio}/C)

151 stoichiometries of the intercepted particles (Fig. 3c). A positive linear relationship (i.e.,
152 similar biogenic flux and regenerative stoichiometries) should be observed if bacterial
153 solubilization exerts a first-order control on DFe resupply. Here, the absence of such a
154 relationship, along with systematically lower DFe replenishment rates relative to P and C
155 (Supplementary-Table 2), confirm that DFe resupply results from a combination of biotic and
156 abiotic transformations of sinking PFe[15,17]. As highlighted in Fig. 3c, dissolution of lithogenic
157 Fe (i.e., DFe release without O_2 consumption) increases $R_{Fe/O2}$ and hence $R_{Fe/C}$, whereas Fe
158 scavenging (i.e., DFe removal without O_2 consumption) has the opposite effect. As expected
159 for areas dominated by biogenic PFe such as the subantarctic, bacterial solubilization
160 explained most of the $R_{Fe/C}$ relative to that of scavenging (Fig. 3c). The relatively large excess
161 in post-incubation Fe-binding ligands (L*) observed at SAZ (Fig. 4), driven by bacterial
162 degradation of biogenic-dominated sinking particles[9,16], is consistent with these low
163 scavenging rates pointing to complex interplay between processes associated with biogenic
164 and lithogenic PFe.
165
166 In contrast, a pronounced mismatch was observed between $R_{Fe/C}$ and the biogenic flux
167 stoichiometry at ALG at the deeper depth (195 m) and both depths at ION (Fig. 3c). Although
168 this trend results from the dominance of particle scavenging over solubilization/dissolution
169 (Fig. 4), the increase of this mismatch with depth may be explained by increasing scavenging
170 and/or decreasing solubilization/dissolution. Saharan dust-derived Fe dissolution rates are
171 reported to remain constant for several days in lab-studies[30], arguing for a relatively constant
172 dissolution rate over this 115-195 m stratum that particles will sink through on this
173 timescale[7,9]. Although changes in the bacterial solubilization rate of PFe, over this depth
174 range, cannot be directly assessed, the increasing proportion of C respired with depth
175 (Supplementary-Table 2) is not consistent with decreased bacterial solubilization rate of PFe

176 (by assuming constant or increasing biogenic Fe/C ratio[15]). Thus, increased scavenging (Fig.
177 4), is the most likely mechanism to account for the trend in $R_{Fe/C}$ with depth.
178
179 Measurements of size and concentration of particles collected at the Mediterranean sites
180 revealed decreasing cumulative particle volume concentrations with depth (Supplementary-
181 Table 4), excluding these two parameters as possible drivers of increased scavenging rate.
182 Therefore, the increase with depth in the relative proportion of lithogenic material being
183 exported (Supplementary-Fig. 2b and f), and the resulting decrease in the release of Fe-
184 binding ligands (Supplementary-Table 3), are most likely jointly responsible for this shift
185 within the upper mesopelagic (115-195 m; ALG/ION) stratum in the balance between
186 remineralization of biogenic PFe (DFe and ligand release), dissolution of lithogenic PFe (DFe
187 release) and scavenging processes. These findings demonstrate the confounding role played
188 by dust-derived lithogenic particles, conventionally viewed as a major pelagic DFe source[2,5],
189 but shown here in the upper 100-200 m stratum to act primarily as a scavenging-modulated
190 sink for DFe, and as a ballasting agent[25,31,32], each influencing where in the water column DFe
191 is replenished.
192
193 **Vertical resetting of mesopelagic biogeochemical conditions** – Figure 4 summarises how
194 the interplay of biogenic and lithogenic processes establish iron biogeochemical conditions at
195 each site, and importantly reset conditions with depth. Biogenic PFe is the main source of
196 DFe replenishment via bacterial solubilization, and this is also the case for the concurrent
197 release of iron-binding ligands. By combining the observations from TM-RESPIRE with
198 dissolution rate and scavenging ratios derived from prior dust-addition studies[18,30], it is
199 evident that lithogenic PFe contributes ~10 times more to Fe scavenging relative to Fe
200 dissolution in the upper mesopelagic (Fig. 4) supporting our observations in Fig. 3c. It is

important to note that high scavenging rates were reported even when L* was (slightly) positive (Fig. 3c and 4). It is probable that the higher the value of L* the less likelihood of pronounced scavenging, however, this trend, of scavenging when L* is positive, points to an unknown or unexplored mechanism (e.g., sorption of complexed Fe, colloidal aggregation). These contrasting biogenic and lithogenic roles point to the importance of the composition of the PFe flux in setting the Fe remineralization length-scale, with high PFe attenuation at the biogenic end-member site, and in contrast an increase in PFe sinking flux at the lithogenic end-member site.

Conceptually, depth-dependant changes in the relative proportion of biogenic vs. lithogenic PFe, driven by their different attenuation length-scales, result in an ongoing resetting of the biogeochemical conditions (e.g., L*, ballasting via changes to the specific gravity of the particle) while particles are settling in the water column (Fig. 4). The vertical trend observed at the ALG site – characterized by intermediate surface characteristics relative to the two other sites (Fig. 1c) – illustrates this dynamic situation. At 115 m depth, bacterial degradation of heterogenous (i.e., biogenic/lithogenic) particles resulted in a relatively high post-incubation L* (Fig. 4) and a low scavenging rate (Fig. 3c and 4). However, 80 m deeper, alteration of the composition of the PFe flux resulted in a decrease in post-incubation L* (Fig. 4; Supplementary-Table 3) and a marked increase in the scavenging rate (Fig. 3c and 4). A similar increase in scavenging with depth was observed at the ION site (Fig. 4). The dynamic interplay between biogenically- and lithogenically-modulated mechanisms explain the unexpected high spatial (and by analogy, temporal) and vertical variability in the PFe remineralization reported in this study, but not so far captured in biogeochemical models[7].

We report a ~thousand-fold range in the DFe replenishment rate, while only modest changes in P and C remineralization rates occurred at all sites (Supplementary-Table 2). At the SAZ, the decoupling between Fe and C remineralization was relatively low and comparable to that reported for sinking diatoms in subtropical waters[15]. In contrast, a pronounced decoupling between Fe and both C and P remineralization was observed at ALG and ION. Critically, the lithogenic component of the sinking flux, by having virtually no influence on C and P remineralization, amplifies the decoupling between the Fe and both the C and P remineralization length-scales. This finding highlights that the multi-faceted effects of particle composition and dynamics on mesopelagic iron recycling needs to be considered in global biogeochemical models, to better explain the spatial variability in the decoupling of nutrient recycling.

Controls on the global iron distribution – The most straightforward route to examining the broader role of biogenic:lithogenic particle composition on iron distributions was to focus on the links to lithogenic iron, as dust supply is a well-established component of iron biogeochemical models[4]. The modelling simulations exploited the observed Fe/O_2 relationship with dust (Fig. 3b-c) to develop a simple first-order parameterization that captures observed links between Fe/O_2 and dust (Fig. 5a). Thus, an additional modulator of Fe remineralization, based on the atmospherically-derived lithogenic particle concentration, was added to the PISCES model parameterization, which enabled the sensitivity of iron biogeochemistry to the impact of lithogenic particles on mesopelagic DFe cycling to be addressed (Methods).

This simulation was employed to assess the wider implications of the multi-faceted roles of lithogenic Fe on ocean iron cycling. Projections of the upper mesopelagic (100-250 m) DFe

inventory, in this amended simulation, decreased by 23.7% relative to the control run (Fig. 5b) and as expected, this trend was especially marked in areas influenced by high dust deposition (i.e., North Atlantic, North Pacific, and Indian Oceans). In parallel, the DFe inventory between 1000-1250 m depth increased by 6.4% across the global ocean (Fig. 5b). Ultimately, the effect of lithogenic particles on PFe remineralization is to deepen the vertical profile of DFe and therefore drive the replenishment of DFe deeper in the water column (Fig. 5c). This significant redistribution of DFe over the upper 1000 m has important ramifications when considering that this depth stratum is heavily influenced by mode and intermediate waters lateral transport[33], which can then alter DFe supply to different ocean regions and the associated primary production (Supplementary-Fig. 4b). Therefore, the vertical redistribution of iron in regions dominated by settling lithogenic particles may be pronounced when changes in dust delivery to the ocean[34] may be accompanied by altered ocean circulation in the coming decades[5].

Our findings suggest that predicted changes in dust inputs[34], by altering the biogenic:lithogenic composition of the sinking particle assemblage, may impact the replenishment of the subsurface DFe inventory and vertical supply of DFe not only in dusty regions, but across the global ocean. This alteration, across many oceanic provinces, of DFe resupply may in return have profound effects on the carbon sequestration efficiency of the biological pump[35]. Our study enhances the wider understanding of the role of dust in altering particle composition which in turn influences the replenishment of the subsurface DFe inventory. This research points to the need for further studies on the internal cycling of trace metals if we are to fully understand how they are returned to surface waters via their biogeochemical cycles.

References

1. Moore, C. M. *et al*. Processes and patterns of oceanic nutrient limitation. *Nat. Geosci.* **6**, 701-710 (2013).
2. Jickells, T. D. *et al*. Global iron connections between desert dust, ocean biogeochemistry, and climate. *Science* **308**, 67-71 (2005).
3. Guieu, C., *et al*. Iron from a submarine source impacts the productive layer of the Western Tropical South Pacific (WTSP). *Sci. Rep.* **8**, 9075 (2018).
4. Tagliabue, A. *et al.* How well do global ocean biogeochemistry models simulate dissolved iron distributions? *Glob. Biogeochem. Cycles* **30**, 149-174 (2016).
5. Tagliabue, A. *et al*. The integral role of iron in ocean biogeochemistry. *Nature* **543**, 51-59 (2017).
6. GEOTRACES Planning Group. GEOTRACES Science Plan. Baltimore, Maryland: Scientific Committee on Oceanic Research (2006).
7. Boyd, P. W., Ellwood, M. J., Tagliabue, A., & Twining, B. S. Biotic and abiotic retention, recycling and remineralization of metals in the ocean. *Nat. Geosci.* **10**, 167-173 (2017).
8. Tagliabue, A. *et al.* Surface-water iron supplies in the Southern Ocean sustained by deep winter mixing. *Nat. Geosci.* **7**, 314-320 (2014).
9. Boyd, P. W., Ibisanmi, E., Sander, S. G., Hunter, K. A., & Jackson, G. A. Remineralization of upper ocean particles: Implications for iron biogeochemistry. *Limnol. Oceanogr.* **55**, 1271-1288 (2010).
10. Ye, Y., Wagener, T., Völker, C., Guieu, C., & Wolf-Gladrow, D. A.. Dust deposition: iron source or sink? A case study. *Biogeosciences* **8**, 2107-2124 (2011).
11. Völker, C., & Tagliabue, A. Modeling organic iron-binding ligands in a three-dimensional biogeochemical ocean model. *Mar. Chem.* **173**, 67-77 (2015).

12. Frew, R. D. *et al.* Particulate iron dynamics during FeCycle in subantarctic waters southeast of New Zealand. *Glob. Biogeochem. Cycles* **20**, GB1S93 (2006).
13. Lamborg, C. H., Buesseler, K. O., & Lam, P. J. Sinking fluxes of minor and trace elements in the North Pacific Ocean measured during the VERTIGO program. *Deep Sea Res. Part II* **55**, 1564-1577 (2008).
14. Ellwood, M. J. *et al.* Pelagic iron cycling during the subtropical spring bloom, east of New Zealand. *Mar. Chem.* **160**, 18-33 (2014).
15. Twining, B. S. *et al.* Differential remineralization of major and trace elements in sinking diatoms. *Limnol. Oceanogr.* **59**, 689-704 (2014).
16. Velasquez, I. B. *et al*. Ferrioxamine siderophores detected amongst iron binding ligands produced during the remineralization of marine particles. *Front. Mar. Sci.* **3**, 172 (2016).
17. Boyd, P. W., & Ellwood, M. J. The biogeochemical cycle of iron in the ocean. *Nat. Geosci.* **3**, 675-682 (2010).
18. Wagener, T., Guieu, C., & Leblond, N. Effects of dust deposition on iron cycle in the surface Mediterranean Sea: results from a mesocosm seeding experiment. *Biogeosciences* **7**, 3769-3781 (2010).
19. Bressac, M., & Guieu, C. Post-depositional processes: What really happens to new atmospheric iron in the ocean's surface? *Glob. Biogeochem. Cycles* **27**, 859-870 (2013).
20. Wuttig, K. *et al*. Impacts of dust deposition on dissolved trace metal concentrations (Mn, Al and Fe) during a mesocosm experiment. *Biogeosciences* **10**, 2583-2600 (2013).
21. Burd, A. B. *et al*. Assessing the apparent imbalance between geochemical and biochemical indicators of meso-and bathypelagic biological activity: What the @$♯! is wrong with present calculations of carbon budgets? *Deep Sea Res. Part II* **57**, 1557-1571 (2010).

22. Boyd, P. W., McDonnell, A., Valdez, J., Lefèvre, D., & Gall, M. P. RESPIRE: An in situ particle interceptor to conduct particle remineralization and microbial dynamics studies in the oceans' Twilight Zone. *Limnol. Oceanogr. Methods* **13**, 494-508 (2015).
23. Albani, S. *et al.* Improved dust representation in the Community Atmosphere Model. *J. Adv. Model Earth Sy.* **6**, 541-570 (2014).
24. Sedwick, P. N., *et al.* Limitation of algal growth by iron deficiency in the Australian Subantarctic region. *Geophys. Res. Lett.* **26**, 2865-2868 (1999).
25. Bressac, M. *et al*. Quantification of the lithogenic carbon pump following a simulated dust-deposition event in large mesocosms. *Biogeosciences* **11**, 1007-1020 (2014).
26. Ternon, E. *et al.* The impact of Saharan dust on the particulate export in the water column of the North Western Mediterranean Sea. *Biogeosciences* **7**, 809-826 (2010).
27. Trull, T. W., Bray, S. G., Manganini, S. J., Honjo, S., & Francois, R. Moored sediment trap measurements of carbon export in the Subantarctic and Polar Frontal Zones of the Southern Ocean, south of Australia. *J. Geophys. Res.* **106**, 31489-31509 (2001).
28. Francois, R., Honjo, S., Krishfield, R., & Manganini, S. Factors controlling the flux of organic carbon to the bathypelagic zone of the ocean. *Glob. Biogeochem. Cycles* **16**, 34-1 (2002).
29. Henson, S. A., Sanders, R., & Madsen, E. Global patterns in efficiency of particulate organic carbon export and transfer to the deep ocean. *Glob. Biogeochem. Cycles* **26**, GB1028 (2012).
30. Wagener, T., Pulido-Villena, E., & Guieu, C. Dust iron dissolution in seawater: Results from a one-year time-series in the Mediterranean Sea. *Geophys. Res. Lett.* **35**, L16601 (2008).

31. Louis, J., Pedrotti, M. L., Gazeau, F., & Guieu, C. Experimental evidence of formation of Transparent Exopolymer Particles (TEP) and POC export provoked by dust addition under current and high pCO_2 conditions. *PloS one* **12**, e0171980 (2017).
32. Pabortsava, K. *et al.* Carbon sequestration in the deep Atlantic enhanced by Saharan dust. *Nat. Geosci.* **10**, 189 (2017).
33. Hanawa, K. & Talley, L. D. in *Ocean Circulation and Climate*. Eds Siedler, G. & Church, J., Academic, San Diego, 373–386 (2001).
34. Mahowald, N. M., & Luo, C. A less dusty future?. *Geophys. Res. Lett.* **30**, 1903 (2003).
35. Blain, S. *et al.* Effect of natural iron fertilization on carbon sequestration in the Southern Ocean. *Nature* **446**, 1070-1074 (2007).

Corresponding author – Correspondence and requests for materials should be addressed to M.B. (matthieu.bressac@utas.edu.au).

Acknowledgements – We thank the captains and crew of the *RV Investigator* and *RV Pourquoi Pas?*, the CSIRO and DT INSU teams for the design and preparation of the mooring line, C. Young and P. Waller for building the TM-RESPIRE. The CSIRO Hydrochemistry team, S. Albani, N. Bhairy, E. Cavan, X. Chan, G. De Liège, J. Derrick, K. Desboeufs, F. D'Ortenzio, A. Dufour, M. Garel, J. Guittonneau, N. Haentjens, S. Helias Nunige, S. Jacquet, P. Jansen, N. Leblond, D. Lefèvre, H. Planquette, C. Ridame, G. Rougier, V. Tallendier, C. Tamburini, A. Tovar-Sanchez and T. Trull are thanked for their help at sea and/or samples analysis. This project was funded by a Marie Sklodowska-Curie Postdoctoral European Fellowship awarded to M.B (European Union Seventh Framework Programme ([FP7/2007-2013]) under grant agreement no. [PIOF-GA-2012-626734] (IRON-IC project)). This study is a contribution to the PEACETIME project (http://peacetime-project.org), a joint

initiative of the MERMEX and ChArMEx components supported by CNRS-INSU, IFREMER, CEA, and Météo-France as part of the programme MISTRALS coordinated by INSU. This study was also partly funded by the Australian Research Council by a Laureate awarded to P.W.B (FL160100131), and Discovery project awarded to M.J.E and P.W.B. (DP170102108).

Author contributions – M.B. designed and carried out the study, analysed the data, and wrote the manuscript. C.G. and P.W.B. helped in the design of the study and co-led the cruises. P.W.B. worked on the different versions of the manuscript. M.J.E., T.W., and E.C.L.C. helped in the different instrument deployments and sampling. M.J.E., and T.W. helped in the analysis of samples. A.T. provided and helped interpret the PISCES model output. H.W. and G.S. analyzed the ligand samples. All authors commented on and contributed to the improvement of the manuscript.

Competing interests – The authors declare no competing interests.

Figure 1. *In situ* particle remineralization measurements at contrasting biogeochemical sites. a, Conceptual alteration of particles within the (TM-)RESPIRE. Sinking particles are intercepted for ~36h and regularly transferred into the inner chamber. Next, particles are immediately incubated for >24h at *in situ* pressure and temperature during which bacterial solubilization (i.e., diminished green particles) releases elements. See Methods for chemical assays, and corrections applied to obtain pre-incubation particulate concentrations. **b**, Typical oxygen optode time-series measured within RESPIRE. Bacterially-mediated remineralization is derived from ΔO_{2max} and Δt (i.e., the time-period where the slope of the linear regression is maximum). **c**, Weekly chlorophyll climatology from Modis-Aqua (green; 2003–2017; 1°x1°

resolution) and monthly climatology of simulated dust deposition (brown; 0.9°x1.25° resolution)[23] in the subantarctic (SAZ: upper-panel), and Mediterranean Sea (ALG: middle; ION: lower-panel). Grey vertical bars are (TM-)RESPIRE sampling periods.

Figure 2. Summary of downward particle fluxes and composition from (TM-)RESPIRE at SAZ (green), ALG (red) and ION (blue). Coloured solid circles denote POC fluxes (mmol m^{-2} d^{-1}; averaged (TM-)RESPIRE fluxes) at each depth (left-hand downward arrow, corresponding to the centre of each circle). PFe fluxes (μmol m^{-2} d^{-1}) are represented by coloured circle rims, and the partitioning of the PFe flux by the proportion of grey (lithogenic) and white (biogenic) within each circle (Methods). All fluxes were corrected for bacterial remineralization during the incubation (Methods). The circle size represents the flux magnitude (Supplementary-Table 1) and are enlarged 10-fold (inside the dashed rectangle) at the low-flux SAZ site. At SAZ, fluxes are the mean of two successive deployments (same depth).

Figure 3. Bacterial particle remineralization and iron regeneration efficiency at SAZ (green), ALG (red) and ION (blue). a, Remineralization versus POC concentrations (corrected for remineralization during the incubation) measured within RESPIRE at 115 m (triangles), 160 m (circles), and 195 m (diamonds). The best-fit of the linear model is plotted. **b**, Regeneration efficiencies ($R_{Fe/O2}$) versus the Fe/C molar ratios of intercepted particles (a proxy for PFe flux composition, higher ratios have more PFe_{litho}; Methods). The best-fit of the power law model is presented. **c**, Fe/C regeneration ratios ($R_{Fe/C}$), obtained from $R_{Fe/O2}$ and a C:O_2 conversion factor (Methods), versus the bulk (open symbols) and biogenic (Fe_{bio}/C; Methods; closed symbols) Fe/C molar ratios. To aid interpretation, Fe-specific processes (vertical arrows) in relation to $R_{Fe/C}$ and Fe_{bio}/C are displayed. The grey triangle illustrates the

421 increasing proportion of lithogenic PFe across sites and with depth. Error bars were derived
422 using uncertainty-propagation laws (Methods). Fluxes were expressed as concentrations to
423 permit cross-comparison between sites (different collection/incubation times employed).
424
425 **Figure 4. Synthesis of key processes that together set the PFe remineralization length-**
426 **scale expressed as a function of the relative proportion of sinking biogenic:lithogenic**
427 **PFe.** Sites and depths are assigned into each of three idealized categories: biogenic-dominated
428 (SAZ), heterogeneous (biogenic/lithogenic; ALG 115 m), and lithogenic-dominated (ALG
429 195 m, ION 115-195 m) PFe fluxes. Note, how intercepted sinking particles at ALG shift
430 categories with depth. For PFe attenuation, + and – denote the magnitude of the decrease or
431 increase in the flux with depth, respectively. Note, the dynamic nature of concurrent ligand
432 release and scavenging as particles settle, means that L*>0 may not impede scavenging (see
433 Fig. 3c). Nevertheless, the higher the value of L* the less likelihood of pronounced
434 scavenging.
435
436 **Figure 5. Results of model simulations using lithogenic particle-dependent modulation of**
437 **iron remineralization. a**, Relationship between $R_{Fe/O2}$ and lithogenic PFe concentrations in
438 offshore regions (>3000 m depth; 30°S-30°N) employing different lithogenic particle-
439 dependent modulators of iron remineralization (kd; Methods). **b**, Change in DFe inventory
440 vertically integrated over 100-250 m (upper-panel) and 1000-1250 m (lower-panel) depth
441 strata relative to the control run. This simulation is based on a 500-year simulation employing
442 a kd of 0.1 μg m^{-3} (i.e., which reproduced the inverse relationship observed between $R_{Fe/O2}$
443 and the lithogenic PFe concentration in panel **a**). **c**, Alteration of the global mean vertical DFe
444 profile from a simulation employing a kd of 0.1 μg m^{-3} relative to the control run.
445

METHODS

Site selection – Datasets were acquired during two GEOTRACES process studies, in the Subantarctic Zone (SAZ) southwest of Tasmania, aboard the *RV Investigator* (March 2017; SOTS project), and in the central (Ionian Sea, ION) and western (Algerian Basin, ALG) Mediterranean Sea aboard the *RV Pourquoi Pas?* (May/June 2017; Peacetime project). Sites were selected for their contrasting magnitude and composition of the downward particle flux. In particular, ~30-fold higher lithogenic fluxes have been reported at ~1000 m depth at ALG (12.7 g m^{-2} yr^{-1})[36] and ION (13.9 g m^{-2} yr^{-1})[37], relative to SAZ (0.4 g m^{-2} yr^{-1})[27]. In contrast, POC fluxes at ~1000 m depth are relatively similar at SAZ (1.1-1.4 g m^{-2} yr^{-1})[38], ALG (1.4-1.7 g m^{-2} yr^{-1})[36], and ION (0.7-0.9 g m^{-2} yr^{-1})[37].

The SAZ represents >50% of the areal extent of the ice-free Southern Ocean. This HNLC area has both low silicate and DFe concentrations year round[24] along with moderate phytoplankton biomass[39]. The low dust flux to this area originates primarily from Australia, with the highest fluxes between October and March[40]. POC (0.91-1.23 mmol m^{-2} d^{-1}) and PFe (0.48-0.67 μmol m^{-2} d^{-1}) fluxes measured in this study compared well with POC (3.34 ± 1.81 mmol m^{-2} d^{-1})[41] and PFe (0.17 ± 0.09 μmol m^{-2} d^{-1})[42] fluxes measured at the same site and depth, but in January/February.

The Mediterranean Sea has a west-to-east gradient of increasing oligotrophy, with a deficiency of phosphorus and nitrogen. Relatively weak winter convection[43] prevents efficient uplift of nutrients to the surface waters. Deposition of Saharan desert dust, characterized by strong variability and dominated by extreme events[44], constitutes the main source of new nutrients. ION is an ultra-oligotrophic area, while the ALG is one of the most productive areas in the Mediterranean Sea[45]. At ALG/ION, POC fluxes measured at 195 m depth (1.14-1.67 mmol m^{-2} d^{-1}) are consistent with previous measurements (0.4-3.0 mmol m^{-2} d^{-1}, $1^{st}/3^{rd}$ quartiles)[46], but ~4-fold higher than fluxes simultaneously measured at 250 m depth with a

PPS5 sediment trap (0.32-0.37 mmol m^{-2} d^{-1}; N. Leblond, pers. comm.). Similarly, 2-fold higher PFe fluxes were collected at 195 m depth with the TM-RESPIRE (13.4-16.1 µmol m^{-2} d^{-1}) compared to PFe fluxes at 250 m depth (PPS5; 4.5-8.5 µmol m^{-2} d^{-1}; N. Leblond, pers. comm.).

(TM-)RESPIRE – The conceptual view, functioning and potential artefacts of the RESPIRE particle interceptor are detailed in ref.[22]. TM-RESPIRE, a trace metal-clean version of RESPIRE, was developed to quantify PFe remineralization rates. TM-RESPIRE is constructed from polycarbonate (PC) except for the PVC indented rotating sphere (IRS), and has identical dimensions to RESPIRE (Supplementary-Fig. 1). The IRS excludes mesozooplankton from the incubation chamber, and delivers particles every ~10 min into this chamber. When the IRS is not rotating, the chamber beneath it is completely closed, avoiding any exchange with the upper part of TM-RESPIRE. Trace metal cleanliness and optode-based oxygen measurements are not reconcilable since plastic material essential for trace elements studies often have high oxygen permeability, and optodes require a metal window. To circumvent these issues, TM-RESPIRE was systematically deployed concurrently with the RESPIRE fitted with an Aanderaa 3830 oxygen optode (resolution < 1 µM; accuracy < 5 µM).

Optodes were post-calibrated using the Winkler method, and oxygen time-series were corrected for pressure and salinity (Aanderaa operating manual). A pressure sensor (RBR, Canada) was deployed alongside RESPIRE to determine the deployment depth. The vertical distance between the TM-RESPIRE and RESPIRE (10-20 m; Supplementary-Table 1) was constrained by the ship's dimensions (i.e., distance above the waterline) and the necessity to keep a minimum distance between the two traps to avoid contamination through contact with the vessels' hull or propeller wash during deployment/recovery.

Remineralization rates measured within the RESPIRE were assumed to be comparable in the TM-RESPIRE. This assumption is supported by similar rates obtained at SAZ after two successive deployments several days apart (5.1 ± 0.2 mmol O_2 m^{-3} d^{-1}; Fig. 3a), and by previous replicate RESPIRE measurements exhibiting small variability in the remineralization rates[47]. In the present study, POC fluxes from RESPIRE and TM-RESPIRE (vertically separated by 10-20 m) varied on average by a factor of 1.8 ± 0.6 (n = 6). Similar POC flux variabilities were observed at ALG/ION (250 m depth) and SAZ (150 m depth) across individual 12-24 h samples obtained by conventional sediment traps which varied on average by 1.6 ± 0.8 (N. Leblond, pers. comm.) and 3[(41)], respectively. This relatively high variability in successive upper mesopelagic POC flux measurements suggests that the differences observed in the present study is driven largely by inherent variability in the POC flux in this stratum[48], rather than by the vertical spacing between the RESPIRE and TM-RESPIRE.

(TM-)RESPIRE procedure – RESPIRE were cleaned following ref.[22]. Before each voyage, TM-RESPIRE were soaked in 2% Neutracon (7d), 2 M HCl (reagent grade; 30d), 1.2 M HCl (TM grade; 7d), and copiously rinsed with Ultrapure water. Before deployment, each TM-RESPIRE was filled overnight with 0.12 M HCl (TM grade), rinsed with Ultrapure water and pre-conditioned with low-Fe filtered seawater to remove all trace of acid. Several hours before deployment, RESPIRE and TM-RESPIRE were filled with filtered seawater collected at the deployment depth. Clean polyethylene (PE) bags covering the traps were removed just prior to deployment. Upon recovery, RESPIRE and TM-RESPIRE were immediately covered with PE bags. TM-RESPIRE's were transferred into a class-100 clean laboratory. Seawater above the IRS was siphoned off using clean Teflon PFA tubing, and the incubation chamber was sampled via a Teflon PFA stopcock valve. The absence of mesozooplankton in the chamber was confirmed by visual inspection. Samples were split into equal fractions and

subsamples for DFe, Fe-binding ligands, and nutrients were filtered through acid-cleaned 0.2-µm PC membranes. DFe samples were stored in low density PE (LDPE) bottles and acidified to pH 1.8 (quartz-distilled HCl). Fe-binding ligand samples were transferred to high density PE bottles (cleaned following GEOTRACES protocols, http://www.geotraces.org/science/science-highlight/intercalibration/222-sampling-and-sample-handling-protocols-for-geotraces-cruises), double-bagged and stored at -20°C. 0.2-µm PC membranes were dried under a laminar flow hood and used for particulate trace element analysis. Subsamples for POC were obtained by filtration onto pre-combusted 13-mm QMA or GF/F filters. RESPIRE was sampled for POC and nutrients. All steps were performed within 2-3 hours of recovery of (TM-)RESPIRE.

TM-RESPIRE procedural blank measurements were performed onboard during voyages. Blanks comprised incubating <0.2-µm seawater from 150 m depth within the TM-RESPIRE. After 72 h, the blank samples were subjected to identical processing protocols (i.e., subsampling, filtration) as for deployments. The average DFe blank (DFe_{blank}; 0.38 ± 0.03 nM) was used to correct DFe release (see Calculation of metrics). However, we acknowledge that deployment and recovery are two steps with high risk of contamination. Concentrations in trace elements other than Fe (such as Zn) measured within the TM-RESPIRE were used to assess possible contamination (not necessarily conspicuous with DFe) that could have occurred during deployment/recovery. This approach allowed us to reject one contaminated deployment (Subantarctic voyage, April 2016).

Water column sampling – Samples were collected using a Titanium Rosette mounted with Teflon-coated 12 L Niskin (SAZ) or Go-Flo bottles (ALG/ION) deployed on a Kevlar cable. After recovery, bottles were transferred inside a class-100 clean laboratory container. Seawater samples were directly filtered from the bottles through acid-cleaned 0.2-µm capsule

546 filters (Sartorius Sartobran-P-capsule 0.45/0.2-µm). DFe samples were stored in LDPE bottles
547 and acidified to pH 1.8 (quartz-distilled HCl), while nutrient samples were analyzed at sea.
548 Suspended particulate trace elements were sampled using in situ pumps (McLane; acid-
549 cleaned 1-µm PC membranes) at SAZ and pressurized Go-Flo bottles at ALG/ION (acid-
550 cleaned 25-mm diameter Supor 0.45-µm polyethersulfone filters; 4.8 L on average) following
551 GEOTRACES recommendations.
552
553 **Analytical methods** – DFe concentrations were measured by flow injection with online
554 preconcentration and chemiluminescence detection[3,49]. An internal acidified seawater
555 standard was measured daily to control the stability of the analysis. During the analysis of
556 TM-RESPIRE and water-column samples, the detection limit was 15 pM and the accuracy of
557 the method was controlled by analyzing the SAFe S (0.086 ± 0.010 nmol/kg (n = 3);
558 consensus value 0.093 ± 0.008 nmol/kg), SAFe D1 (0.64 ± 0.13 nmol/kg (n = 19); consensus
559 value 0.67 ± 0.04 nmol/kg), GD (1.04 ± 0.10 nmol/kg (n = 10); consensus value 1.00 ± 0.10
560 nmol/kg), and GSC (1.37 ± 0.16 nmol/kg (n = 4); consensus value not available) seawater
561 standards.
562 Dissolved nutrients were analysed onboard with a segmented flow analyser (AAIII HR Seal
563 Analytical; detection limits were 0.02 µM for P, 0.05 µM for N, and 0.08 µM for Si) [50,51].
564 Iron organic speciation measurements were performed using CLE-CSV with 2-(2-
565 Thiazolylazo)-p-cresol (TAC) as the competing ligand[52]. Reagent blanks for Fe were
566 undetectable and the detection limit for ligand concentrations was calculated as 3 times the
567 standard deviation of the concentrations (ranging from 0.09-0.99 nM and always lower than
568 the concentration).
569 Particulate trace element samples were digested (10% HF/50% HNO_3 (v/v)) following the
570 protocol described in the "GEOTRACES Cookbook" and ref.[53]. Procedural blanks consisted

571 of unused acid-cleaned filters. Analyses were performed on a high resolution ICP-MS
572 (Element XR, Thermo-Fisher Scientific). The accuracy of the measurements was established
573 using a range of Certified Reference Materials, including MESS-4. The recoveries in these
574 reference materials were 80-130% for iron.
575 POC samples were acidified overnight with 2 M HCl to remove inorganic C, and then dried at
576 60°C for 2 d. Samples were analyzed on a CHN analyser (Thermo Finnigan EA 1112 Series
577 Flash Elemental Analyser).
578
579 **Calculations of metrics** – Mesozooplankton, free-living and particle-attached heterotrophic
580 bacteria drive mesopelagic remineralization[54]. By excluding mesozooplankton (using the IRS)
581 and boosting particle-attached bacterial abundances relative to free-living bacteria (through
582 particle interception), the measured remineralization rates were dominated by the particle-
583 attached microbial assemblage[22].
584 **Particle remineralization** was calculated as follows: the pre-incubation O_2 concentration
585 (Fig. 1b) was subtracted from each data-point obtained during the incubation, and the sign
586 reversed. The slope of the linear regression between this remineralization signature and the
587 time elapsed corresponds to the particle remineralization rate. Note that the decrease in O_2
588 was not systematically linear, and a plateau can be attained toward the end of the incubation
589 (Fig. 1b). The explanation for this trend remains unclear, but may be related to particle
590 containment, a shift in the microbial community[55], and/or altered organic matter lability[22].
591 When such a plateau was evident, remineralization was calculated over the time period where
592 the decrease in O_2 was maximum (Fig. 1b). Since remineralization rates were assumed to be
593 comparable within the RESPIRE and TM-RESPIRE, the error in remineralization rates was
594 calculated by propagating the uncertainty from the slope of the linear regression and the
595 relative standard deviation of the POC fluxes collected by the RESPIRE/TM-RESPIRE. The

596 error in ΔO_2 (see below) was calculated in the same way.

597 **The iron regeneration efficiency** ($R_{Fe/O2}$; μmol/mol; Fig. 3b) was calculated as: $R_{Fe/O2}$ =
598 $\Delta DFe / \Delta O_2$, where $\Delta DFe = DFe_{post\text{-}incubation} - (DFe_{initial} + DFe_{blank})$, and $\Delta O_2 = O_{2\ pre\text{-}incubation} -$
599 $O_{2\ post\text{-}incubation}$ (initial, pre-incubation, and post-incubation terms are illustrated in Fig. 1a). The
600 error in $R_{Fe/O2}$ was calculated by propagating the uncertainties from ΔDFe and ΔO_2.

601 **The Fe/C regeneration ratio** ($R_{Fe/C}$; μmol/mol; Fig. 3c) was calculated as: $R_{Fe/C} = R_{Fe/O2} /$
602 0.69, where 0.69 is a C:O_2 conversion factor (i.e., 117/170)[56]. Note that different conversion
603 factors can be used to convert the oxygen-based remineralization rate to carbon (discussed in
604 detail in ref.[22]).

605 **Particulate fluxes were expressed as concentrations** to permit cross-comparison between
606 sites in which different collection times were employed (Supplementary-Table 1). **Pre-**
607 **incubation particulate Fe, P, and OC concentrations** correspond to the sum of the post-
608 incubation particulate concentration, plus the concentration of the respective element released
609 into the dissolved phase (i.e., ΔDFe, ΔPO_4 (= $PO_{4\ post\text{-}incubation} - PO_{4\ initial}$), and ΔOC (= $\Delta O_2 \times$
610 0.69), respectively).

611 **The replenishment rate of Fe** (% d^{-1}; Supplementary-Table 2) was calculated as: (ΔDFe /
612 $PFe_{pre\text{-}incubation}$) × 100 / Δt, (Δt corresponds to the incubation time). The error was calculated
613 by propagating the uncertainties from ΔDFe and $PFe_{pre\text{-}incubation}$. P and C replenishment rates
614 were calculated in the same way.

615 **Quantification of the lithogenic and biogenic fractions of sinking PFe** has large
616 uncertainties. Twining et al.[15] reported a 2.3 and 4.4-fold increase in the Fe/P and Fe/S (proxy
617 of Fe/C) ratios of sinking diatom by 200 m depth, respectively, highlighting difficulties in
618 estimating the biogenic fraction of sinking PFe from surface cell quotas. An alternative
619 approach is to estimate the lithogenic fraction of PFe by using the Fe/Al ratio. However, the
620 present study encompasses different regions where lithogenic material has different Fe and Al

compositions. In addition, dissolution/scavenging of Fe and Al differ during particle settling[60], altering their pre-depositional Fe/Al ratio. Thus, lithogenic PFe estimated at ALG/ION using a Saharan dust end-member Fe/Al ratio[59] is systematically higher than total PFe. In contrast, suspended particles collected at ALG/ION had a Fe/Al ratio comparable to the crustal Fe/Al ratio[58] (Supplementary-Fig. 3). Thus, the crustal Fe/Al molar ratio was used to estimate biogenic and lithogenic PFe components in Fig. 2 and 3c. For the remainder of the study, the PFe/POC molar ratio (hereafter termed Fe/C) of the intercepted particles (Fig. 3) was used as a proxy for the composition of the PFe flux. In using this approach, we consider POC and PFe as proxies of biogenic (algal/detrital) and lithogenic PFe, respectively[9]. This ratio increases when the relative proportion of lithogenic Fe increases, and vice-versa. We acknowledge that the biogenic Fe/C ratio differs between Fe-limited and Fe-replete areas, however, we believe that this approach is relatively robust when considering such contrasting sites.

Ancillary biogeochemical information – Surface chlorophyll-*a* was derived from MODIS-Aqua. The 4 km resolution eight-day composite images were averaged over the 2003-2017 period (due to extensive subantarctic cloud-cover) for a 1°x1° box centered at each site. At SAZ, MODIS chlorophyll-*a* concentrations were corrected using an improved regional algorithm[61].

Monthly estimates of total (wet + dry) dust deposition annually averaged were obtained using an atmospheric model (CAM4-BAM, case C4fn)[23] run for 30 years, of which we considered the last 10 years, with a spatial resolution of 0.9°x1.25°.

The PISCES biogeochemical model experiment – PISCES[62,63] is a relatively complex general ocean circulation and biogeochemistry model with two PFe pools (large and small)

characterized by different sinking rates, and two analogous POC size classes sourced from the 'mortality' of organic Fe and C pools. Uncomplexed DFe is subjected to scavenging, while colloidal iron undergoes coagulation losses, both of which augment two PFe size classes. Scavenging rate depends on the particle abundance, including the lithogenic PFe pool (based on the dust input at the surface and a simple sinking speed). Subsurface dissolution of lithogenic PFe occurs with a ~500 m length-scale, a sinking rate of 2 m d^{-1}, and a reduced solubility. PFe remineralization takes into account changes in particle size and lability due to bacterial solubilization via reactivity continuum[64].

We conducted a range of different simulations with PISCES aimed at addressing the first-order influence of lithogenic particles (i.e., dust) on $R_{Fe/O2}$. Building this parameterization on dust has many advantages. Indeed, biogenic Fe is a complex pool (detritus/algal) characterized by different cell quotas[65], while dust supply is a well-established component[4] that does not require explicit modelling of extra pools and can be incorporated more widely into models. In the model, $R_{Fe/O2}$ is derived by dividing the annually integrated remineralization flux of iron from PFe by the O_2 consumption during remineralization at each model grid cell. We conducted a set of sensitivity experiments where PFe remineralization was modulated by the lithogenic particle concentration at each model grid cell. This modulator (M, an unitless quantity) is a function of the lithogenic particle concentration: M = 1 – [lithogenic particles / (lithogenic particles + kd)]. M has a range of different sensitivities (kd = 0.1, 1, 5 and 10 μg m^{-3}). To avoid double accounting, Fe scavenging by dust included in PISCES[62] was switched off. We then ran for 500 years experiments as well as a 500-year model run in which PFe remineralization was left unchanged (Supplementary-Fig. 4a). We then compared the range of $R_{Fe/O2}$ outputs from each experiment with the local lithogenic PFe concentrations (Fig. 5a), which showed that kd = 0.1 μg m^{-3} was the most realistic as it reproduced the inverse relationship observed between $R_{Fe/O2}$ and the lithogenic PFe

671 concentrations (Fig. 3b). To minimize the impact of high iron inputs (e.g., near shelves), only
672 offshore regions (>3000 m depth; 30°S-30°N) were considered. Finally, the impact of this
673 new parameterization on DFe inventories, vertical DFe distribution, and surface iron-driven
674 processes was investigated.
675
676 **Exploration of caveats** – Our approach comes with some caveats, most of which were
677 identified and discussed in ref.[22]. Here, we discuss potential biases that may have affected Fe
678 cycling within the TM-RESPIRE. Specifically, we acknowledge that the pre-concentration of
679 particles in a 1.6 L chamber, along with the widely-differing downward fluxes (Fig. 2), may
680 have influenced the DFe replenishment rates.
681 The potential effects of this experimental bias, related to the need of concentrating particles
682 and to the contrasting sites, were tested via *in vitro* incubation experiments (Supplementary-
683 Fig. 5). The rationale, method, and conclusions are described in the Figure caption. Results
684 from these experiments suggest that during the <48 h incubation within the TM-RESPIRE,
685 the limited loss of DFe by adsorption onto walls/particles was not significantly influenced by
686 the particle concentration, and by the surface-area-to-volume (SA:Vol) ratio of the incubation
687 bottles (0.31-0.59 cm^{-1}). This later finding allows us to conclude that a different SA:Vol ratio
688 of the TM-RESPIRE incubation chamber (0.57 cm^{-1}) would not have changed our
689 conclusions.
690 In our study, the concomitant decreases in DFe replenishment and particle volume
691 concentrations observed with depth at ALG/ION (Supplementary-Tables 2 and 4) do not
692 support a particle concentration effect on the replenishment of Fe. This experimental bias, that
693 would act to lower DFe concentration, has mainly been observed during dust dissolution
694 experiments[66]. This effect is likely offset in incubations with mixed biogenic/lithogenic
695 particles (along with the associated bacterial communities) by the concurrent release of Fe-

696 binding ligands (which increased on average by a factor >2 in our study; Supplementary-
697 Table 3). Consistent with the conclusions of this study, the particle composition and/or
698 bacterial communities, rather than experimental parameters, appear to be the primary control
699 of the DFe replenishment rate in these *in vitro* experiments.
700
701 **Data availability** – Modis Chl-a concentrations (ALG and ION sites) were obtained with the
702 Giovanni online data system, developed and maintained by the NASA GES DISC. MODIS
703 Chl-a concentrations corrected using an improved regional algorithm for the Southern Ocean
704 (SAZ site) are publicly available via the Australian Integrated Marine Observing System
705 (IMOS) Ocean Portal (www.imos.org.au). Following publication, the dataset generated and
706 analysed during the current study (mostly available in the Supplementary Information section)
707 will be made available (i.e. open access) through the IMAS/UTAS data portal
708 (http://www.imas.utas.edu.au/data).
709
710 **Code availability** – The NEMO-PISCES model we use in this work is freely available
711 (http://www.nemo-ocean.eu/) under the CeCILL free software licence
712 (http://www.cecill.info/index.en.html). We used a modified version of the PISCES
713 biogeochemical model. These modifications concern the representation of the particulate iron
714 remineralization and this is not yet present in the freely available NEMO release but will be
715 provided upon contacting A.T.
716
717 **References**
718 36. Zúñiga, D., et al. Particulate organic carbon budget in the open Algero-Balearic Basin
719 (Western Mediterranean): Assessment from a one-year sediment trap experiment. *Deep*
720 *Sea Res. Part I* **54**, 1530-1548 (2007).

721 37. Stavrakakis, S., *et al*. Downward fluxes of sinking particulate matter in the deep Ionian
722 Sea (NESTOR site), eastern Mediterranean: seasonal and interannual variability.
723 *Biogeosciences* **10**, 7235 (2013).
724 38. Rigual-Hernández, A. S., Trull, T. W., Bray, S. G., & Armand, L. K. The fate of diatom
725 valves in the Subantarctic and Polar Frontal Zones of the Southern Ocean: Sediment trap
726 versus surface sediment assemblages. *Palaeogeogr. Palaeoclimatol. Palaeoecol.* **457**,
727 129-143 (2016).
728 39. Eriksen, R., *et al*. Seasonal succession of phytoplankton community structure from
729 autonomous sampling at the Australian Southern Ocean Time Series (SOTS) observatory.
730 *Mar. Ecol. Prog. Ser.* **589**, 13-31 (2018).
731 40. Li, F., Ginoux, P., & Ramaswamy, V. Distribution, transport, and deposition of mineral
732 dust in the Southern Ocean and Antarctica: Contribution of major sources. *J. Geophys.*
733 *Res.* **113**, D10207 (2008).
734 41. Ebersbach, F., Trull, T. W., Davies, D. M., & Bray, S. G. Controls on mesopelagic
735 particle fluxes in the Sub-Antarctic and Polar Frontal Zones in the Southern Ocean south
736 of Australia in summer—Perspectives from free-drifting sediment traps. *Deep Sea Res.*
737 *Part II* **58**, 2260-2276 (2011).
738 42. Bowie, A. R. *et al*. Biogeochemical iron budgets of the Southern Ocean south of
739 Australia: Decoupling of iron and nutrient cycles in the subantarctic zone by the
740 summertime supply. *Glob. Biogeochem. Cycles*, **23**, GB4034 (2009).
741 43. D'Ortenzio, F., *et al.* Seasonal variability of the mixed layer depth in the Mediterranean
742 Sea as derived from in situ profiles. *Geophys. Res. Lett.* **32**, L12605 (2005).
743 44. Guerzoni, S., *et al*. The role of atmospheric deposition in the biogeochemistry of the
744 Mediterranean Sea. *Progr. Oceanogr.* **44**, 147-190 (1999).

745 45. D'Ortenzio, F., & Ribera d'Alcalà, M. On the trophic regimes of the Mediterranean Sea: a
746 satellite analysis. *Biogeosciences* **6**, 139-148 (2009).
747 46. Ramondenc, S., et al. An initial carbon export assessment in the Mediterranean Sea based
748 on drifting sediment traps and the Underwater Vision Profiler data sets. *Deep Sea Res. Part I* **117**, 107-119 (2016).
750 47. McDonnell, A. M., Boyd, P. W., & Buesseler, K. O. Effects of sinking velocities and
751 microbial respiration rates on the attenuation of particulate carbon fluxes through the
752 mesopelagic zone. *Glob. Biogeochem. Cycles* **29**, 175-193 (2015).
753 48. Lamborg, C. H., *et al*. The flux of bio-and lithogenic material associated with sinking
754 particles in the mesopelagic "twilight zone" of the northwest and North Central Pacific
755 Ocean. *Deep Sea Res. Part II* **55**, 1540-1563 (2008).
756 49. Bonnet, S., & Guieu, C. Atmospheric forcing on the annual iron cycle in the western
757 Mediterranean Sea: A 1-year survey. *J. Geophys. Res. Oceans* **111**, C09010 (2006).
758 50. Rees, C., *et al*. Methods for reproducible shipboard SFA nutrient measurement using
759 RMNS and automated data processing. *Limnol. Oceanogr. Methods* **17**, 25-41 (2019).
760 51. Aminot, A., & Kérouel, R. Dosage automatique des nutriments dans les eaux marines:
761 méthodes en flux continu, Ed. Ifremer, Méthodes d'analyse en milieu marin (2007).
762 52. Croot, P. L. & Johansson, M. Determination of Iron Speciation by Cathodic Stripping
763 Voltammetry in Seawater Using the Competing Ligand 2-(2-Thiazolylazo)-p-cresol
764 (TAC). *Electroanalysis* **12**, 565-576 (2000).
765 53. Planquette, H., & Sherrell, R. M. Sampling for particulate trace element determination
766 using water sampling bottles: methodology and comparison to in situ pumps. *Limnol. Oceanogr. Methods* **10**, 367-388 (2012).
768 54. Steinberg, D. K., *et al*. Bacterial vs. zooplankton control of sinking particle flux in the
769 ocean's twilight zone. *Limnol. Oceanogr.* **53**, 1327-1338 (2008).

55. LeCleir, G. R., DeBruyn, J. M., Maas, E. W., Boyd, P. W., & Wilhelm, S. W. Temporal changes in particle-associated microbial communities after interception by nonlethal sediment traps. *FEMS microbiol. Ecol.* **87**, 153-163 (2014).

56. Anderson, L. A., & Sarmiento, J. L. Redfield ratios of remineralization determined by nutrient data analysis. *Glob. Biogeochem. Cycles* **8**, 65-80 (1994).

57. Reinthaler, T., *et al*. Prokaryotic respiration and production in the meso-and bathypelagic realm of the eastern and western North Atlantic basin. *Limnol. Oceanogr.* **51**, 1262-1273 (2006).

58. Wedepohl, K. H. The composition of the continental crust. *Geochim. Cosmochim. Acta* **59**, 1217-1232 (1995).

59. Guieu, C., Loÿe-Pilot, M. D., Ridame, C., & Thomas, C. Chemical characterization of the Saharan dust end-member: Some biogeochemical implications for the western Mediterranean Sea. *J. Geophys. Res.* **107**, ACH-5 (2002).

60. Baker, A. R., Adams, C., Bell, T. G., Jickells, T. D., & Ganzeveld, L. Estimation of atmospheric nutrient inputs to the Atlantic Ocean from 50° N to 50° S based on large-scale field sampling: Iron and other dust-associated elements. *Glob. Biogeoch. Cycles* **27**, 755-767 (2013).

61. Johnson, R., Strutton, P. G., Wright, S. W., McMinn, A., & Meiners, K. M. Three improved satellite chlorophyll algorithms for the Southern Ocean. *J. Geophys. Res.* **118**, 3694-3703 (2013).

62. Aumont, O., Ethé, C., Tagliabue, A., Bopp, L., & Gehlen M. PISCES-v2: an ocean biogeochemical model for carbon and ecosystem studies, *Geoscientific Model Development*, **8**, 2465-2513 (2015).

63. Völker, C., & Tagliabue, A. Modeling organic iron-binding ligands in a three-dimensional biogeochemical ocean model, *Mar. Chem.*, **173**, 67-77 (2015).

64. Aumont, O., *et al*. Variable reactivity of particulate organic matter in a global ocean biogeochemical model, *Biogeosciences*, **14**, 2321-2341 (2017).

65. Boyd, P. W. *et al*. Why are biotic iron pools uniform across high-and low-iron pelagic ecosystems?. *Glob. Biogeoch. Cycles* **29**, 1028-1043 (2015).

66. Bonnet, S., & Guieu, C. Dissolution of atmospheric iron in seawater. *Geophys. Res. Lett.* **31**, L03303 (2004).

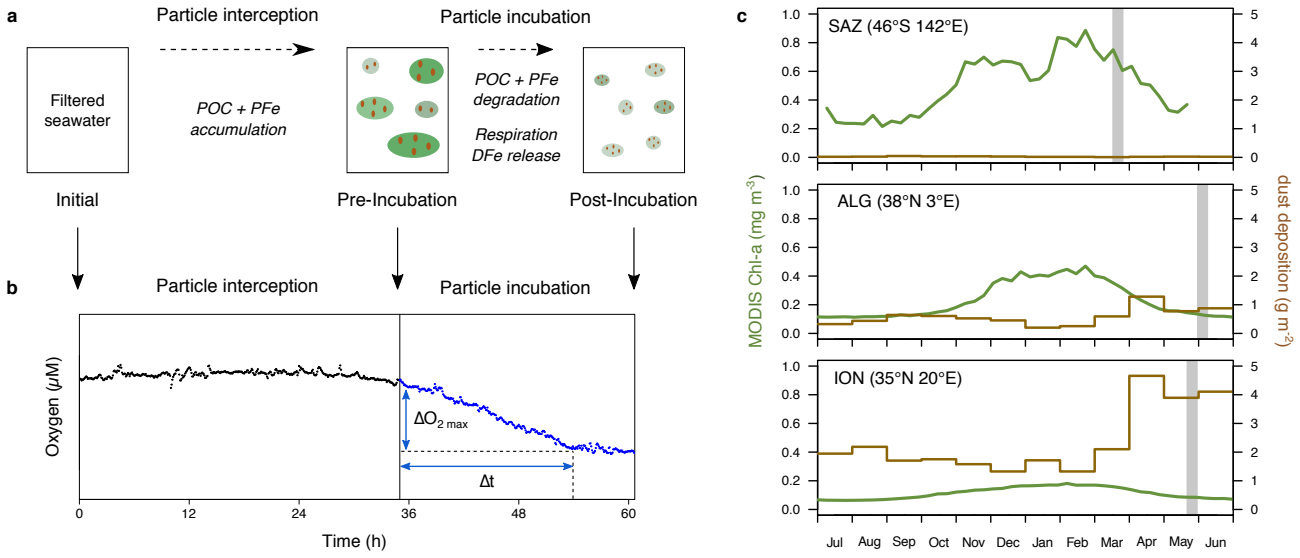
a
Particle interception
Particle incubation
Filtered seawater
POC + PFe accumulation
POC + PFe degradation
Respiration DFe release
Initial
Pre-Incubation
Post-Incubation
b
Particle interception
Particle incubation
Oxygen (μM)
ΔO2 max
Δt
0
12
24
36
48
60
Time (h)
c
SAZ (46°S 142°E)
ALG (38°N 3°E)
ION (35°N 20°E)
MODIS Chl-a (mg m-3)
dust deposition (g m-2)
Jul
Aug
Sep
Oct
Nov
Dec
Jan
Feb
Mar
Apr
May
Jun

SAZ
ALG
ION
100 m
150 m
200 m
x10
x10

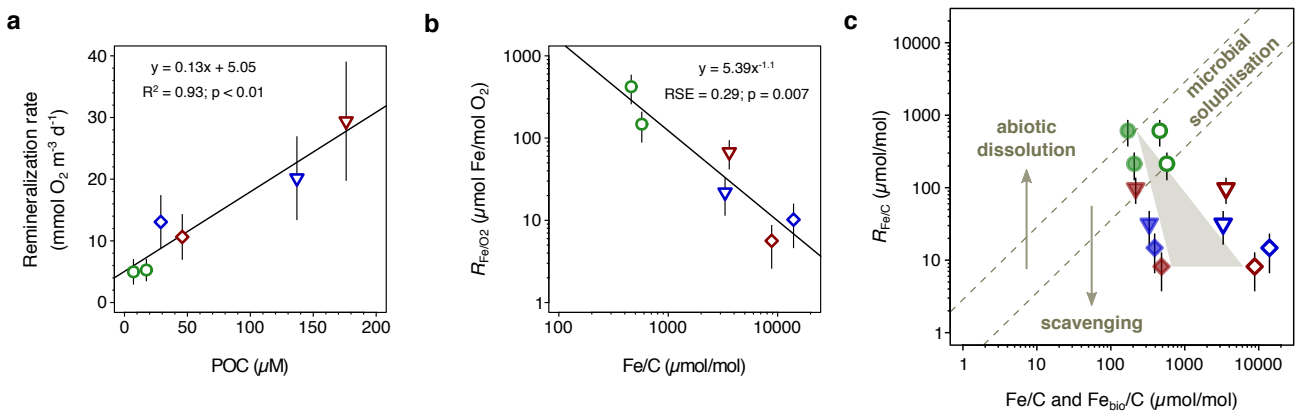
a
y = 0.13x + 5.05
R² = 0.93; p < 0.01
Remineralization rate
(mmol O2 m-3 d-1)
POC (μM)
b
y = 5.39x-1.1
RSE = 0.29; p = 0.007
RFe/O2 (μmol Fe/mol O2)
Fe/C (μmol/mol)
c
abiotic
dissolution
microbial
solubilisation
scavenging
RFe/C (μmol/mol)
Fe/C and Febio/C (μmol/mol)

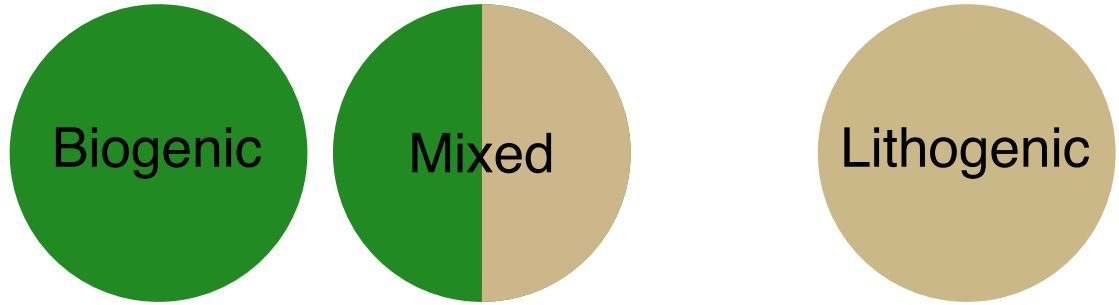

	SAZ	ALG 115 m	→	ALG 195 m	ION 115-195 m
DFe release (μmol Fe/mol O_2)	150-420	68	→	6	22-10
DFe_{litho} [1] (% of ΔDFe)	0.01%	0.5%	→	17%	2-9%
Post-incubation L* [2]	0.43	0.25	→	0.18	0.21-0.12
Potential lithogenic scavenging [3] (% of ΔDFe)	0.3%	5%	→	170%	30-130%
PFe attenuation [4]	(+++)		(-)		(- - -)

(1) Estimates based on a dissolution rate of 0.018 nmol mg^{-1} dust d^{-1} [30]
(2) L* corresponds to the excess of ligands over DFe after the incubation phase
(3) Estimates based on a scavenging ratio of DFe on dust of 0.37 nmol mg^{-1} [18]
(4) At SAZ, estimate based on the balance between DFe/L release and scavenging

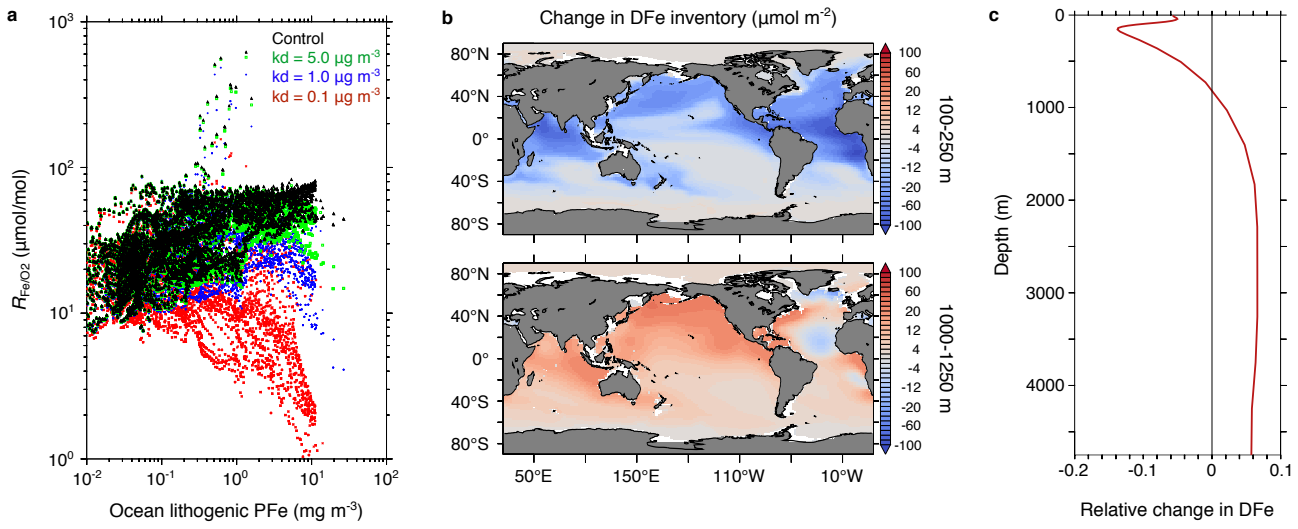
a
Control
kd = 5.0 µg m-3
kd = 1.0 µg m-3
kd = 0.1 µg m-3
RFe/O2 (µmol/mol)
Ocean lithogenic PFe (mg m-3)
b
Change in DFe inventory (µmol m-2)
100-250 m
1000-1250 m
80°N
40°N
0°
40°S
80°S
50°E
150°E
110°W
10°W
c
Depth (m)
Relative change in DFe